


Article

Impact of May–June Antarctic Oscillation on July–August Heat-Drought Weather in Yangtze River Basin

Zhengxuan Yuan ¹, Jun Zhang ², Liangmin Du ^{1,*}, Ying Xiao ¹ and Sijing Huang ³ ¹ Wuhan Regional Climate Center, Wuhan 430074, China; 1201410533@cug.edu.cn (Z.Y.)² China Yangtze Power Co., Ltd., Yichang 443000, China³ School of Environmental Science, China University of Geosciences, Wuhan 430078, China

* Correspondence: duliangmin@outlook.com

Abstract: Investigating the physical mechanism behind the formation of summer heat-drought weather (HDW) in the Yangtze River Basin (YRB) holds significant importance for predicting summer precipitation and temperature patterns in the region as well as disaster mitigation and prevention. This study focuses on spatiotemporal patterns of July–August (JA) HDW in the YRB from 1979 to 2022, which is linked partially to the preceding May–June (MJ) Antarctic Oscillation (AAO). Key findings are summarized as follows: (1) The MJ AAO displays a marked positive correlation with the JA HDW index (HDWI) in the southern part of upper YRB (UYRB), while showing a negative correlation in the area extending from the Han River to the western lower reaches of the YRB (LYRB); (2) The signal of MJ AAO persists into late JA through a specific pattern of Sea Surface Temperature anomalies in the Southern Ocean (SOSST). This, in turn, modulates the atmospheric circulation over East Asia; (3) The SST anomalies in the South Atlantic initiate Rossby waves that cross the equator, splitting into two branches. One branch propagates from the Somali-Tropical Indian Ocean, maintaining a negative-phased East Asia–Pacific (EAP) teleconnection pattern. This enhances the moisture flow from the Pacific towards the middle and lower reaches of the Yangtze River Basin (MYRB–LYRB). The other branch propagates northward, crossing the Somali region, and induces a positive geopotential height anomaly over Urals–West Asia. This reduces the southwesterlies towards the UYRB, thereby contributing to HDW variabilities in the region. (4) Partial Least Squares Regression (PLSR) demonstrated predictive capability for JA HDW in the YRB for 2022, based on Southern Ocean SST.

Keywords: Yangtze River Basin; heat-drought weather; Antarctic oscillation; Southern Ocean; equatorial crossing



Citation: Yuan, Z.; Zhang, J.; Du, L.; Xiao, Y.; Huang, S. Impact of May–June Antarctic Oscillation on July–August Heat-Drought Weather in Yangtze River Basin. *Atmosphere* **2024**, *15*, 998. <https://doi.org/10.3390/atmos15080998>

Academic Editors: Nina Nikolova and Martin Gera

Received: 21 June 2024

Revised: 15 August 2024

Accepted: 16 August 2024

Published: 20 August 2024

Correction Statement: This article has been republished with a minor change. The change does not affect the scientific content of the article and further details are available within the backmatter of the website version of this article.



Copyright: © 2024 by the authors. Licensee MDPI, Basel, Switzerland. This article is an open access article distributed under the terms and conditions of the Creative Commons Attribution (CC BY) license (<https://creativecommons.org/licenses/by/4.0/>).

1. Introduction

Owing to global climate change, the Yangtze River Basin (YRB) has witnessed an increase in the frequency and severity of extreme weather events such as coupled high temperatures and droughts (HDW) in recent years [1–7], indicating a potential new climatic norm [8,9] and inflicting significant adverse effects on human society [10–12]. Notably, the YRB, China’s crucial agricultural hub, has endured severe HDW events in 1994, 2001, 2006, 2011, 2013, 2019, and most notably in 2022 [7,13–16]. In summer 2022, the impact of HDW was particularly widespread, with the highest temperature in its historical records, coupled with minimal precipitation and a record-high number of hot days. This resulted in crop yield declines, diminished river water supply during the flood season, soaring power grid loads, and numerous forest fires in various YRB regions [1,17]. During summer 2022 in the YRB, the positive evapotranspiration anomaly compared with the climatic period (summer of analyzing time period) ranked second since 1960, below the record set in 2013 [18].

The concurrent occurrence of intense drought and persistent high temperatures is a key measure of HDW [19,20]. For instance, in 2013, the HDW in the YRB was influenced by

the East Asia–Pacific (EAP) teleconnection pattern, which was further amplified by the Silk Road teleconnection pattern. This led to an anomalous development of the western Pacific subtropical high (WPSH), subsequently shaping the HDW conditions in the YRB [21]. A rare HDW event occurred in the YRB during summer 2022, tracing back to the enhancement and westward extension of the WPSH in preceding mid-June, as well as its merger with continental high pressure, which was very similar to the climatic background of HDW in the region of Jianghuai during summer 1994 [13]. Meanwhile, the anomalous southward shift of summer tropical convection in 2022 caused anomalous descending motion over the MYRB and LYRB, coupled with an anomalous weak subtropical summer monsoon [22,23]. These factors contributed to widespread positive potential height anomalies across the YRB during late summer, accompanied by stagnant westerly circulation over Eurasia and a weakened low-pressure system over the Qinghai–Tibet Plateau. As a consequence, the water vapor transport in the YRB was dominated by diffusion, and typhoon activities were relatively subdued [18,24,25].

The two notable HDW events in 2013 and 2022 were closely associated with global sea surface temperature (SST) anomalies. In 2013, the anomalous warm SST in the North Atlantic led to a northward shift of the westerly jet stream, thereby intensifying the HDW in the MYRB and LYRB. In contrast, in 2022, an anomalous wave train originating from the North Atlantic propagated eastward, triggering extensive trough and ridge activities. This culminated in the formation of a blocking high-pressure system characterized by “two ridges and one trough” in the Eurasian mid-high latitudes, spanning from the Urals to the Okhotsk Sea. This blocking system maintained cold air above 50° N while simultaneously interacting with the subtropical system, causing flooding in northern China and drought in southern China. Additionally, disturbances over the Qinghai–Tibet Plateau extended the South Asian High eastward, merging it with the WPSH, which directly encompassed most of southern China, thereby intensifying the underlying HDW [26–28]. It is noteworthy that the transition of the North Atlantic Oscillation (NAO) from a positive to a negative phase from the preceding winter to the following summer also contributed to continuous heatwaves in Zagreb, Croatia [29]. Besides the North Atlantic, persistent La Niña events, the negative phase of the tropical Indian Ocean Dipole (TIOD), and the persistent negative snow cover anomaly in the northwest of the Tibetan Plateau in the preceding spring may also be important factors that potentially influenced the anomalous atmospheric circulation in the YRB during summer 2022 [18,25].

Apart from anomalous systems in the Northern Hemisphere, researchers have established a significant causal link between the Southern Hemisphere and the East Asian summer monsoon [30–32]. After eliminating the potential influence of ENSO, the signal of the Antarctic Oscillation (AAO) has persisted seasonally through underlying SST anomalies and subsequently propagates across the equator via the Mascarene High and other mechanisms [33]. This propagation reaches the Northern Hemisphere, modulating the western Pacific subtropical high (WPSH) and its adjacent convection activity, further affecting the circulation in eastern China and consequently influencing temperature and precipitation patterns in the region [34–36]. This lag–lead relationship reflects the predictive significance of the Southern Hemisphere for HDW in the YRB. Recent studies have also shown that the Maritime continent convection induced by the second mode of the atmospheric circulation in the southern hemispheric sub-tropics (STO) in spring drives the EAP teleconnection pattern, which further modulates summer precipitation, and subsequently, HDW in central YRB [37]. Here, the correlation between the southern hemisphere and HDW in the YRB is constructed.

Although preceding AAO may induce variations in precipitation and temperature in Southern China, the detailed mechanism of cross-equatorial and lagging impact of preceding AAO on late HDW in the YRB remains controversial to some extent, as the leading time of AAO to summer HDW in the YRB and the teleconnection patterns between them are still unclear. Clarifying this mechanism within statistical methods, dynamical analysis, and numerical product applications will provide a scientific basis for improving the prediction

capacities of the composite weather-climate events and the further understanding of inter-hemispheric interactions. The structure of the subsequent content is outlined as follows: Chapter 2 discusses the data and methods, Chapter 3 presents the results and discussion, and Chapter 4 concludes the findings. It is noteworthy that the seasons referred to in this study are based on boreal seasons.

2. Data and Methods

2.1. Data

The dataset utilized in this study primarily comprises monthly averages, encompassing wind fields (U , V , units: m/s), vertical velocity (Ω , units: Pa/s), temperature (T , units: $^{\circ}\text{C}$), and geopotential height (H , units: m^2/s^2). These data are sourced from the NCEP/NCAR Reanalysis, originating from the National Oceanic and Atmospheric Administration (NOAA) [38]. The horizontal resolution of these data is $2.5^{\circ} \times 2.5^{\circ}$, and the vertical resolution spans 17 layers. Additionally, this study employs NOAA Extended SST V5 for sea surface temperature (SST) data, covering the period from January 1979 to December 2022.

In the following figures, geopotential height at 500 hPa is denoted as (H500), wind field at 850 hPa is denoted as 'UV850', wind field with geopotential height at same and different altitude are denoted as 'UVH500' and 'H500 UV850', respectively. Water vapor flux at 850 hPa is denoted as 'WF850'. Stream function at 500 hPa is denoted as 'STRF500' while wave flux at 500 hPa is denoted as 'WAF500'. This style of abbreviation applies equally to the other altitudes.

Daily observational data for temperature and precipitation at 700 stations within the Yangtze River Basin (YRB) are provided by the Hubei Meteorological Service (The applied stations are plotted in Figure 1 below), within the time period from 1979 to 2022. Furthermore, the Antarctic Oscillation Index (AAOI) and the Nino3.4 index are obtained from NOAA, with a time range that aligns with the reanalysis data. For the convenience of following analysis, the schematic diagram of YRB is shown as below, referring to the Figure 1 of a previous study [15], as established in Figure S1.

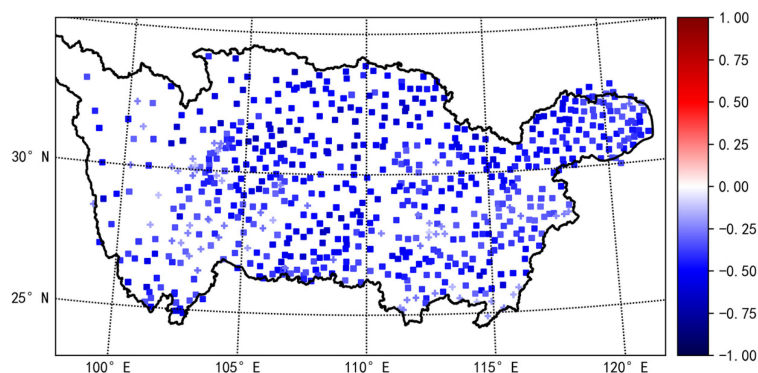


Figure 1. Correlation coefficients between JA SPI90 and JA HDWI in YRB based on observational stations (marker 'square' denotes statistically significant at 95% confidence level, markers 'plus' are insignificant stations).

2.2. Method

2.2.1. Statistical Methods and Machine Learning Methods

The least squares method (LS) is used to calculate the linear regression equation between the sequences X and Y : $Y = AX + B$, in which X denotes a standardized time series and Y denotes the dependent factor. 'A' represents the slope, which indicates that for every unit increased in X , Y increases by 'A' units.

The Empirical Orthogonal Function (EOF) method can be used to analyze the spatiotemporal patterns of meteorological, hydrological and acoustic data matrices. The

characteristic vectors in the analysis results correspond to spatial modes, while time series represent the temporal variations of spatial modes.

The Partial Least Squares (PLS) method [39], a machine learning technique, is utilized in this study to verify the lagged impact of anomalous Southern Hemisphere oceanic conditions on the spatial distribution and trend of summer HDW in the YRB. The PLS regression model aims to decompose the leading modes of contemporaneous matrices X and forecast sequence Y and explain as much of the covariance between X and Y as possible.

2.2.2. Butterworth Filters and Effective Degrees of Freedom

The Butterworth filter, which is widely applied to weather data analysis and has robust filtered results, is used in this study [40] in order to highlight the interannual variabilities of the data, and high-pass filters were applied to which (station values, grid values, and index values) to retain interannual variabilities with the removal of periods over 10 years.

When conducting correlation analysis on these data, the significance test of the correlation coefficient based on effective degrees of freedom (N_{eff}) was adopted to improve accuracy, as shown in Equation (1) [41]:

$$N_{eff} = N / (1 + 2 \sum_{i=1}^{10} a_i b_i) \tag{1}$$

N denotes the sample length, a_i and b_i denote the auto-correlation coefficients of order i^{th} of two time series respectively.

2.2.3. Solve the Rossby Wave Flux and Its Zonal Channel Crossing

T-N flux (TNF) is used to characterize long wave perturbations in non-uniform air flow [42], thereby reinforcing the remote statistical relationship between regions, with the following formula including zonal (TNF_x : Equation (2)) and meridional (TNF_y : Equation (3)) components:

$$TNF_x = \frac{p_0 \cos \varphi}{2|U|} \left[\frac{U}{a^2 \cos^2 \varphi} \left[\left(\frac{\partial \psi'}{\partial \lambda} \right)^2 - \psi' \frac{\partial^2 \psi'}{\partial \lambda^2} \right] + \frac{V}{a^2 \cos \varphi} \left[\frac{\partial \psi'}{\partial \lambda} \frac{\partial \psi'}{\partial \varphi} - \psi' \frac{\partial^2 \psi'}{\partial \lambda \partial \varphi} \right] \right] + Cu \tag{2}$$

$$TNF_y = \frac{p_0 \cos \varphi}{2|U|} \left[\frac{U}{a^2 \cos \varphi} \left[\frac{\partial \psi'}{\partial \lambda} \frac{\partial \psi'}{\partial \varphi} - \psi' \frac{\partial^2 \psi'}{\partial \lambda \partial \varphi} \right] + \frac{V}{a^2} \left[\left(\frac{\partial \psi'}{\partial \varphi} \right)^2 - \psi' \frac{\partial^2 \psi'}{\partial \varphi^2} \right] \right] + Cu \tag{3}$$

φ is latitude, λ is longitude, a is the radius of the Earth, $p_0 = p/1000$. $|U|$ is the horizontal flow amplitude, U and V are the climatological meridional and zonal wind velocity, respectively. ψ' is the anomaly of the stream function. Cu equals 0 based on the assumption of quasi-stationary waves. The stream function is reduced by 10^7 times when plotting.

The meridional wave number across the equator of the Rossby wave can be calculated from the dispersion relation of partial horizontally nonuniform flow (PHNF) [43–45], as shown in Equations (4) and (5):

$$\overline{q_y} = \frac{2\Omega \cos^2 \varphi}{a} - \frac{\cos \varphi}{a^2} \frac{d}{d\varphi} \left[\frac{1}{\cos \varphi} \frac{d}{d\varphi} (\overline{u} \cos \varphi) \right] \tag{4}$$

$$\omega = \overline{u_M} k + \overline{v_M} l + \frac{\overline{q_y} k}{K^2} \tag{5}$$

$\overline{u_M}$ and $\overline{v_M}$ represent the zonal wind and meridional wind velocity under Mercator projection, respectively. $(\overline{u_M}, \overline{v_M}) = (\overline{u}, \overline{v}) / \cos \varphi$. k and l are the zonal wave number and meridional wave number, ω is the dispersion relation of PHNF, $K^2 = k^2 + l^2$. In the dispersion relation formula, the solution for the meridional wave number l can be regarded as propagation solutions (three real roots) and reflection solutions (one real root and two complex roots). The positive real root of the propagation solution represents the northward

propagation of the meridional component of the planetary wave, while the negative one represents southward propagation.

2.2.4. Definition of HDWI

The summer HDW index (HDWI) of YRB is defined by daily observational data from July–August 1979 to 2022. The calculation method for HDWI is based on the sum of the difference between standardized monthly mean air temperature (T_{std}) and standardized monthly mean precipitation (Pr_{std}), and the standardized corresponding month's high temperature days (Dt_{hd} : daily maximum temperature above 35 °C, with no precipitation). The HDWI is defined based on the definition of wet-cold index in Southern China [46–49], as shown in Equation (6):

$$HDWI = T_{std} - Pr_{std} + Dt_{hd} \quad (6)$$

Furthermore, in comparison to the simultaneous Standardized Precipitation Index of 90 days averaged (SPI90), which serves as a measurement of meteorological drought [12,24], late summer (July–August) is highlighted as the key season for following analysis. Monthly precipitation and temperature variabilities are shown in Figure S2, showing that June to September have average no-precipitation days of 15, 17, 18, and 18, and high-temperature days of 2, 7, 6, and 1, respectively, confirming July and August as the peak months for HDW occurrence. In addition, a previous study [7] had pointed out that in the monsoon region of central-eastern China, HDW occurred most frequently during July to August. Therefore, from a qualitative perspective and over longer time scales, JA HDWI could reflect variations of coupled heat and drought in the YRB during late summer.

In July–August from 1979 to 2022, HDWI demonstrated a substantial correlation with SPI90 and effectively illustrated the coupled heat-drought event by taking into account both the average temperature and the number of high-temperature days (Figure 1).

3. Results

3.1. Climatic and Oceanic Background of HDW in the YRB

The analysis of the HDWI in the Yangtze River Basin (YRB) revealed that the first three EOF modes accounted for nearly 72% of the total variance. Specifically, the first mode, contributing 49% of the variance, exhibited a consistent pattern that mirrored the HDW across the entire YRB, which accurately captured two typical years of HDW, 2013 and 2022 (Figure 2a). The second and third modes accounted for approximately 23% of the total variance, respectively, corresponding to the north–south dipole distribution and the east–west dipole distribution of the upper YRB (UYRB) and the MYRB-LYRB (Figure 2b,c).

Furthermore, the correlation coefficient between the time series of the third mode (The third principal component: PC3) and the preceding May–June of AAO (MJ AAO) is 0.375, significant at the 95% confidence level. It is clear that the positive phase of MJ AAO corresponds to the positive anomaly of JA PC3 in western UYRB, as well as the negative anomaly in the northeastern part of the MYRB to LYRB.

To quantify the impact of MJ AAO on JA HDW in the YRB, the correlation field of MJ AAO and JA HDWI of each observational station in the YRB is calculated and shown on Figure S3. The distribution of such correlation coefficient fields closely mirrors that established in Figure 2c. The MJ AAO correlated JA HDWI in the UYRB and MLYRB are denoted as U-HDWI and ML-HDWI by averaging the JA HDWI in the regions of southwestern UYRB [100–105° E, 25–29° N] and northeastern MYRB to LYRB [110–120° E, 30–35° N], respectively. From linear regression results, the slopes for U-HDWI and ML-HDWI of MJ AAO are 0.45 and −0.31, respectively, indicating 1-unit increase of MJ AAO may favor 0.45-unit strengthened HDW in the southwestern UYRB coupled with 0.31-unit weakened HDW in the northeastern MYRB to LYRB within a standardized scale (the average of 0 and the standard deviation of 1). The slopes are both statistically significant at 90% confidence levels according to *p*-value testing following the removal of linear trends and ENSO, and after high-pass filtering, based on effective degrees of freedom.

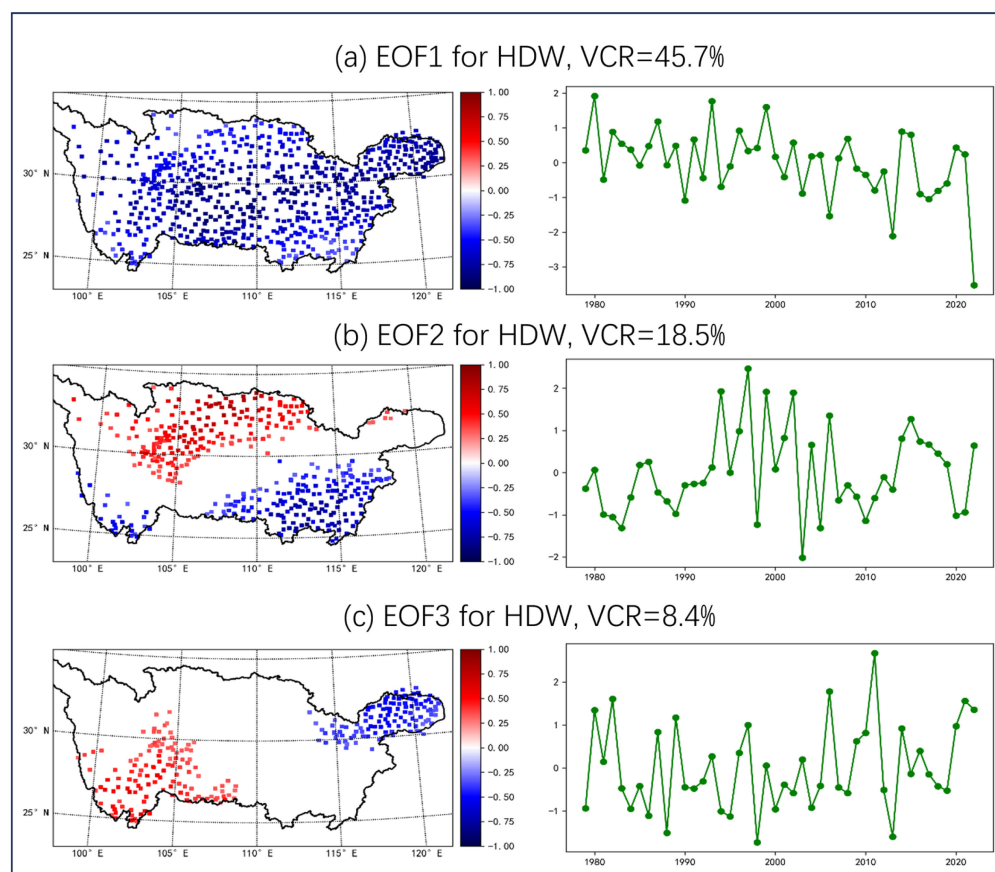


Figure 2. Spatiotemporal modes for EOF results of Jul-Aug HDWI in Yangtze River Basin from 1979 to 2022 ((a). EOF1, (b). EOF2, (c). EOF3. The left columns are spatial patterns as correlation coefficients while the right columns are principal components of each spatial pattern. VCR denotes Variance Contribution Rate).

To clarify the underlying mechanisms for the consideration of MJ AAO, a thorough analysis of the corresponding background circulation and sea surface temperatures (SSTs) associated with JA PC3 was conducted. After high-pass filtering and the removal of linear trends, ENSO effects, and interdecadal trends from JA PC3 and its corresponding grid points, the correlation between JA PC3 and these background grid points was assessed.

Regarding global atmospheric circulation (Figure 3a–c), a notable positive phase of the Antarctic Oscillation (AAO) was observed, particularly over the South Atlantic and South Pacific. From these regions, two northward-propagating wave train branches emerged (Figure 3a,b). These wave train patterns extended from the tropical North Atlantic to East Asia, manifesting as a ‘zonal pattern’ that induced the formation of an East Asia–Pacific (EAP) teleconnection pattern extending from northeast China to Japan (Figure 3e).

Over the East Asian continent (Figure 3d–f), the EAP pattern contributed to the weakening of the westerly jet stream and the dominance of anomalous northeasterlies in the middle-lower Yangtze River Basin (MYRB-LYRB). Accompanied by a cyclonic anomaly, moisture from the Pacific was transported into the MYRB-LYRB, favoring precipitation conditions. Consequently, the intensity of HDW in the MYRB-LYRB is relatively subdued. In contrast, the upper Yangtze River Basin (UYRB) was dominated by positive geopotential height anomalies, particularly over the western part of UYRB. The positive potential height anomaly to the north and the negative anomaly to the east further facilitated the invasion of high-latitude cold air, weakening the northward transport of moist southwesterlies. This led to a lack of favorable precipitation conditions in the UYRB, where the intensity of HDW was relatively strong.

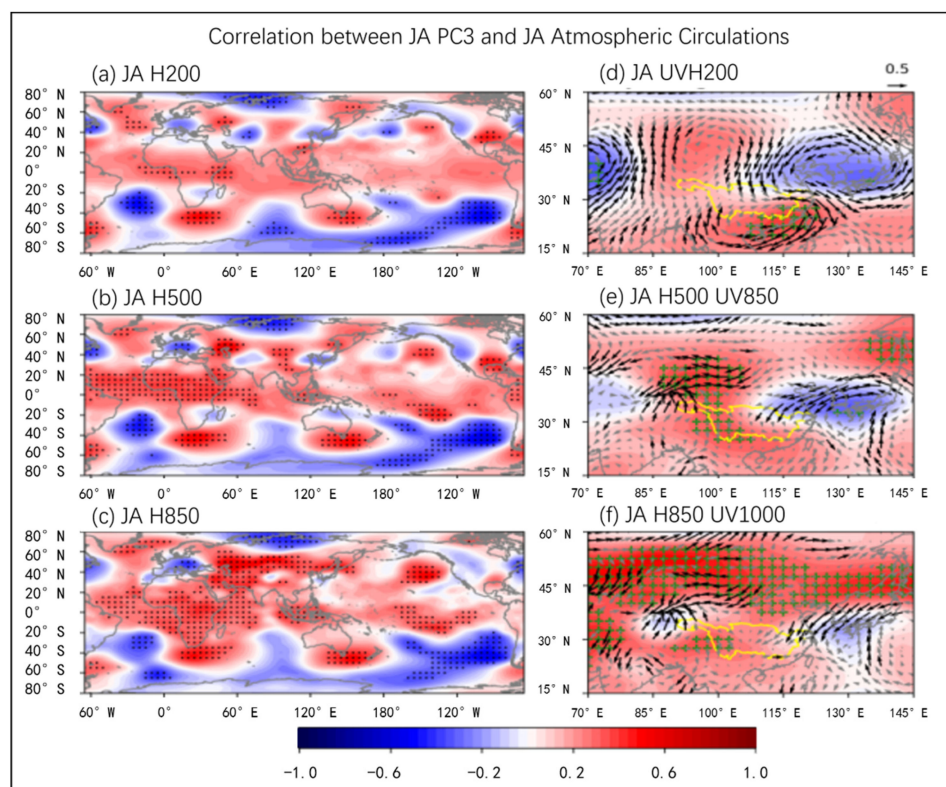


Figure 3. Correlation coefficients July–August PC3 in Yangtze River Basin from 1979 to 2022 and simultaneously atmospheric circulation ((a) for H200, (b) for H500, (c) for H850, dotted regions are statistically significant at 90% confidence level; (d) for UV200H200, (e) for UV850H500, (f) for UV1000H850, green ‘+’ and black vectors are statistically significant at 90% confidence level).

The correlation field between JA PC3 and the concurrent Southern Atlantic dipole and Southern Pacific SST anomaly is statistically significant, which are collectively referred to as the Southern Ocean Sea Surface Temperature Mode (SOSST) in this study (Figure 4).

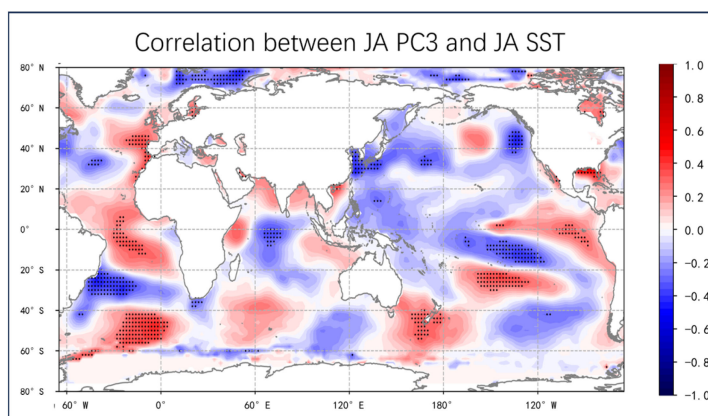


Figure 4. Correlation coefficients between July–August PC3 in Yangtze River Basin from 1979 to 2022 and simultaneously SST (dotted regions are statistically significant at 90% confidence level).

3.2. Mechanism of AAO Influencing the HDW in the YRB

The preceding spring AAO could be prolonged across seasons by underlying surfaces [28,34,50,51]. To determine the correlation between preceding AAO and underlying surfaces, the correlation coefficients between the MJ AAO and contemporaneous as well as lagged JA SSTs (both excluding the decadal signal and the influence of ENSO) are calculated (Figure 5). The results indicate that the Southern Ocean serves as a storage pool for the

persistence of MJ AAO, with the SOSST being significantly established by the ‘oceanic memory’ [47,48,50,52,53]. Therefore, the difference between the area-averaged Atlantic (60° W– 0°) SST at 50° S, coupled with that of southwest Pacific (160° E– 180°) at 40° S, and the area-averaged Atlantic (60° W– 0°) SST at 30° S was standardized to denote the index of SOSST (SOSSTI). The correlation coefficients between the MJ AAO and contemporaneous and lagged JA SOSSTI are 0.302 and 0.470, respectively, both significant at 95% confidence level. Furthermore, the correlation coefficient between JA SOSSTI and concurrent PC3 is 0.411, significant at the 99% confidence level. These correlations highlight the Southern Ocean’s crucial role as a ‘bridge’ of ocean–atmosphere coupling, connecting the AAO and PC3. Additionally, given the chaotic nature of atmospheric signals, JA SOSST can serve as a cross-seasonal indicator of the MJ AAO.

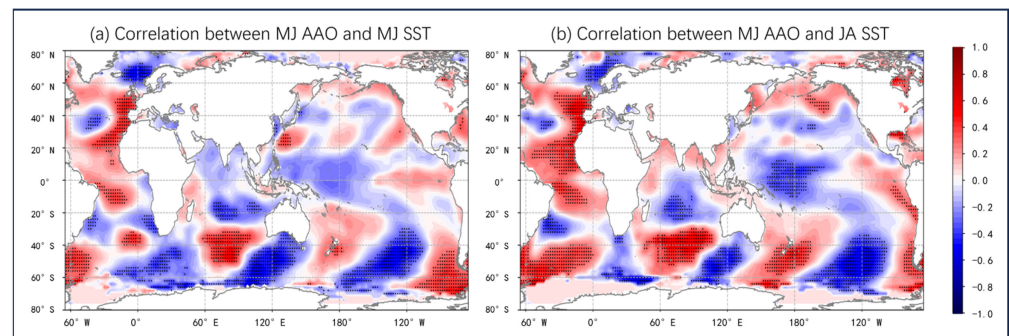


Figure 5. Correlation coefficients between May–June AAO and simultaneously to following SST from 1979 to 2022 (As Figure 3, (a) for May–June SST, (b) for July–August SST).

Typically, the signal of the South Hemisphere traverses the equator to influence the North Hemisphere in two primary manners: through the equatorial symmetry of the regional Hadley circulation, and via the cross-equatorial planetary wave propagation. In this study, we observe a triangular structure formed by the key regions of SOSST and the YRB, though it can be difficult to analyze the linkage between SOSST and YRB through regional meridional-vertical cells for statistical purposes. Meanwhile, previous research has determined the role of regional meridional-vertical cells in the interactions between the two hemispheres [40,54,55], thus, our focus lies in analyzing the planetary wave based on the horizontal profile.

According to the solution of cross-equatorial meridional wave flux in PHNF and TN01, it is evident that wave trains originating in the South Atlantic propagate northeastward (Figure 6). The wave train dissipates into two branches (Figure 6a,b). One branch propagates directly northward, crossing the equator through a channel located over the tropical African continent and its western coast. The other branch propagates northeastward from above Somalia, converging over the western tropical Indian Ocean, specifically the Arabian Sea. Furthermore, anomalous convergence and divergence of these wave trains are also observed over the South Pacific, and with regard to the cross-equatorial tunnel (Figure 6c,d), the tunnel of tropical Indian Ocean and South Africa spanning nearly half of the hemisphere under the adjustment of SOSST (starting from tropical Africa continent and extending eastward to Maritime continent).

It can be inferred that the planetary wave induced by the SOSST variability propagates across the equator and adjusts the northern hemisphere atmospheric circulation. The correlation between SOSSTI and the simultaneous circulation and water vapor flux shows that the water vapor flux diverges over UYRB and converges along with negative geopotential height anomalies over the MYRB-LYRB (Figures 7 and 8). Meanwhile, long-wave disturbances originating from the South Atlantic affect the maintenance of the negative phased EAP teleconnection, resulting in the northerly anomaly in the eastern part of China (Figure 7a,b,d,e). Within the weakening of southward invasion of cold air from high latitudes (Figure 7c,f), the main source of moist conditions in the MYRB-LYRB is the

Pacific (Figure 8a). On the contrary of the UYRB, the lack of moist condition, coupled with positive geopotential height anomaly over the Urals to the Middle East (Figure 7b,c), favors the southeast invasion of high latitudinal cold air flow, reduces the southwest monsoon (Figure 7e), more unfavorable for the convergence of water vapor in UYRB (Figure 8b).

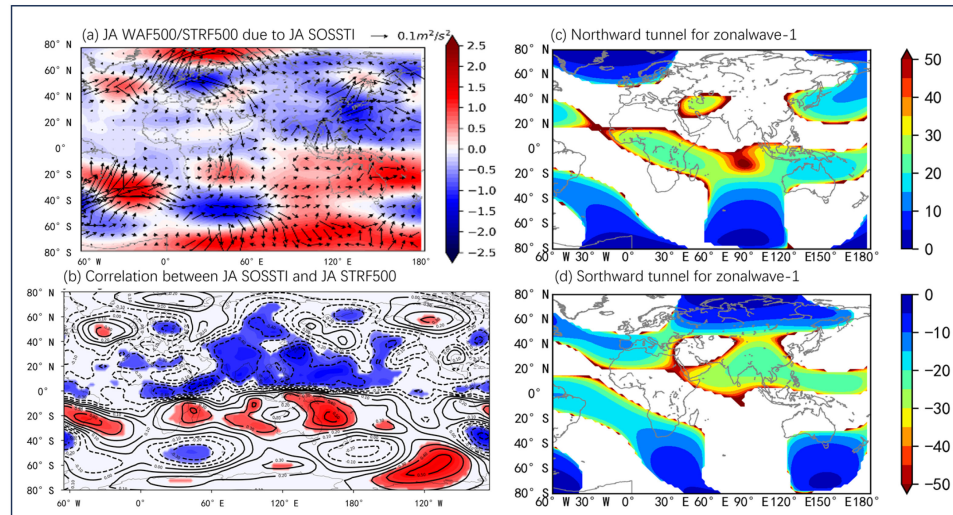


Figure 6. (a) TN flux at 250 hPa induced by the variation of JA SOSSTI (vectors denote wave flux, colors denote streamfunction (STRF)). (b) correlation between JA SOSSTI and JA STRF500 (color shaded regions are significant at 90% confidence level). (c,d) Meridional wave tunnels induced by the variation of JA SOSSTI ((c) for northward tunnel, (d) for southward tunnel).

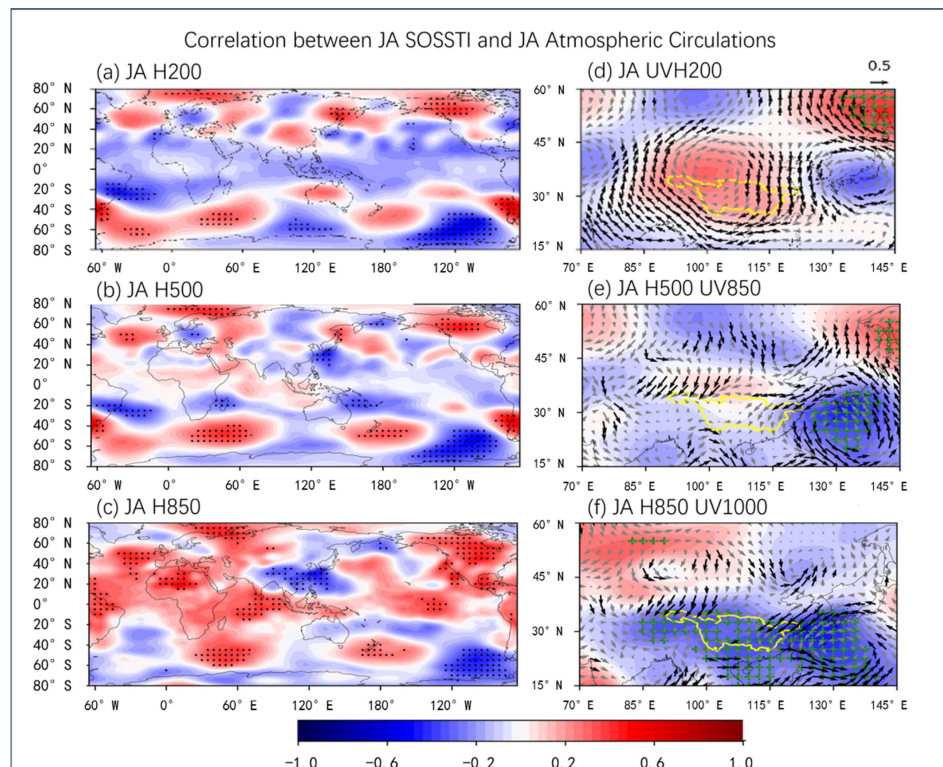


Figure 7. Correlation coefficients July–August SOSSTI from 1979 to 2022 and simultaneously atmospheric circulation ((a) for H200, (b) for H500, (c) for H850, dotted regions are statistically significant at 90% confidence level; (d) for UV200H200, (e) for UV850H500, (f) for UV1000H850, green ‘+’ and black vectors are statistically significant at 90% confidence level).

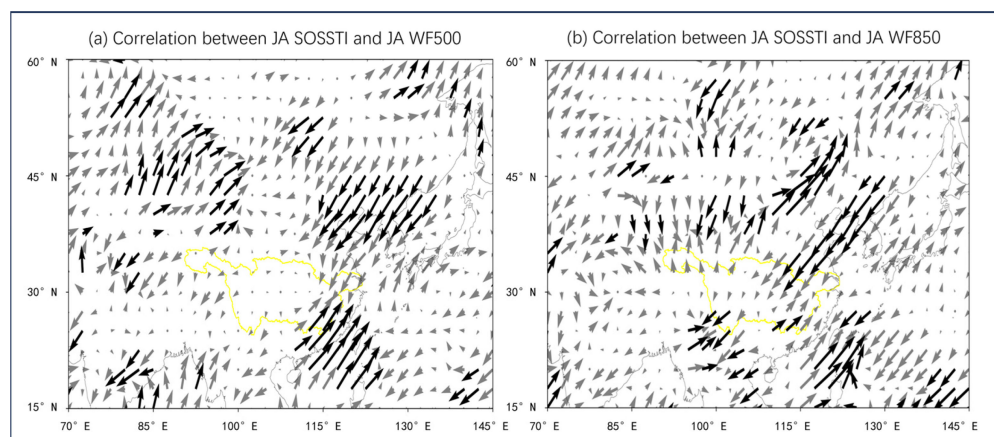


Figure 8. Correlation between JA SOSSTI and simultaneous water vapor flux ((a) 500 hPa; (b) 850 hPa, black vectors are significant at 90% confidence level).

3.3. Predictability of SOSST for the HDW in the YRB

In this section, the PLS method is applied to extract signals from the Southern Ocean to predict the summer HDWI in the YRB. The fit process shows that three of the four leading modes of Southern Ocean SST have significant correlations with the South Atlantic (Figure 9). The first and second modes (Figure 9a,b) show projections of the AAO on the SOD and SAP modes in the Southern Ocean [47,48,56,57]. Predictive results show that the PLS model for the Southern Ocean has good prediction capabilities for the HDW in the YRB during summer 2022 (Figure 10), with an anomaly consistency rate of 97.76%, indicating an in-phased correlation between predicted results and real-time observations of HDWI in YRB. This further confirms that the Southern Ocean has an impact on the moisture and temperature conditions in the YRB during summer.

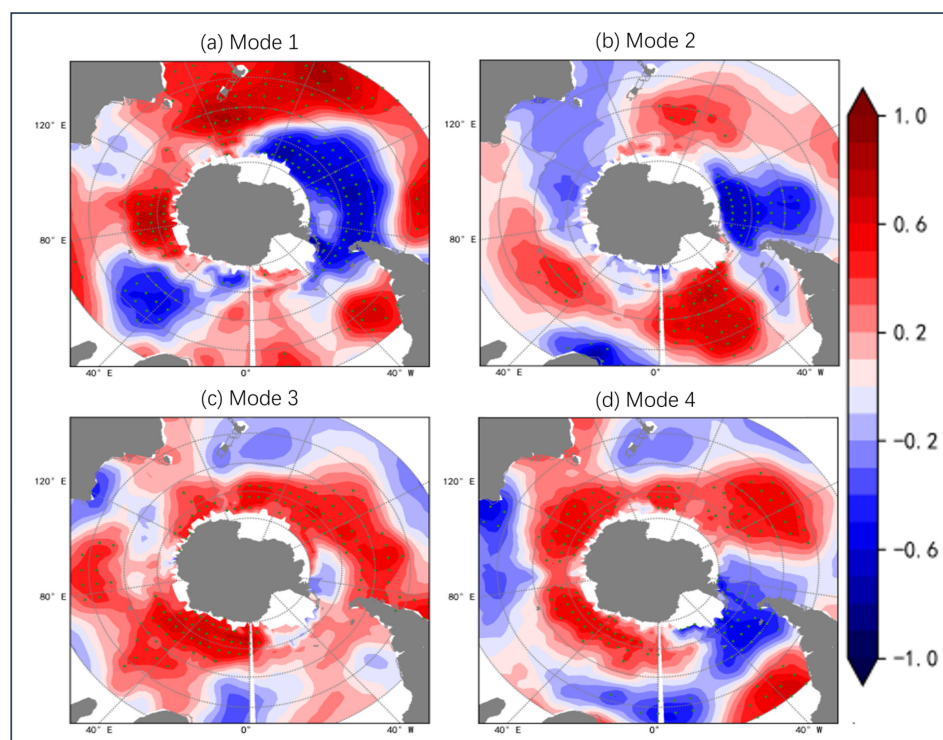


Figure 9. PLS leading modes for the prediction of JA HDW in the YRB by JA SST in Southern Ocean ((a) for mode 1, (b) for mode 2, (c) for mode 3, (d) for mode 4, dotted regions are significant at 90% confidence level).

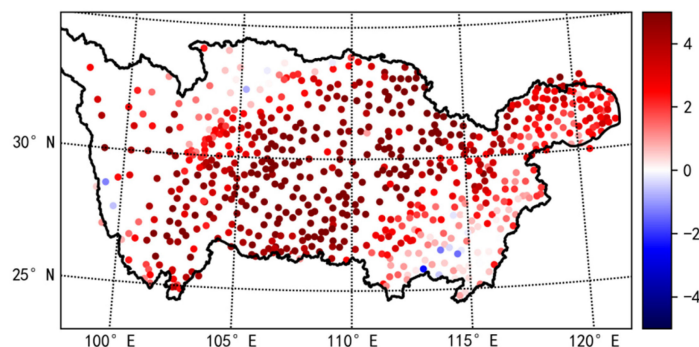


Figure 10. PLS predictive result of JA HDW in the YRB during 2022.

To ensure the robustness for the impact of SOSST to HDW in the YRB, the Australian Community Climate and Earth System Simulator-Earth System Model includes land and ocean carbon cycle components (ACCESS-ESM1-5) with historical periods from 1981 to 2014. The relationship between the SOSST and East Asian atmospheric circulation patterns is validated. To highlight this correlation, the Singular Value Decomposition (SVD) is employed, revealing a pronounced association between JA SOSST and the simultaneous atmospheric circulation of East Asia, as evidenced by the third mode (with the covariance fraction of 4%) of global SST and the Northern Hemisphere's H500 patterns (cps. Figures 5a, 7b and 11).

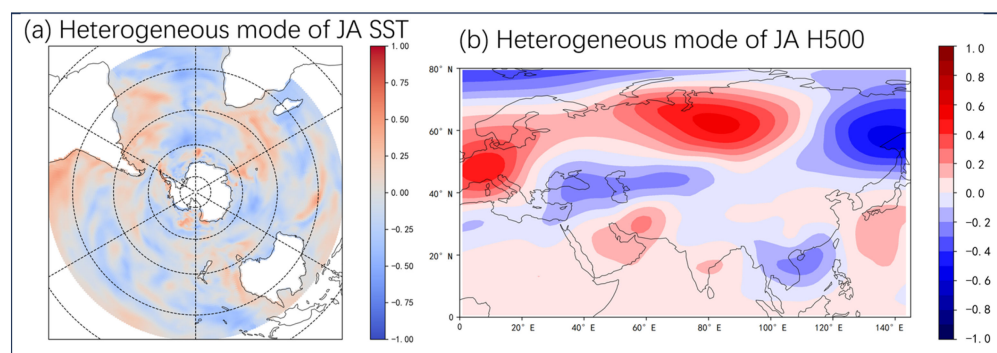


Figure 11. The 3rd heterogeneous mode of global JA SST and northeast hemispheric JA H500 ((a) SST; (b) H500).

In addition to the linear aspect of PLS analysis, the Support Vector Regression (SVR) method is applied for the consideration of a nonlinear relationship between JA SOSST and JA HDW in the YRB. According to the SVR results (Figure S4), the anomaly consistency rate is 80.4%, less than the PLS results. This may suggest that the relationship between SOSST and HDW in the YRB is more linear than nonlinear.

4. Conclusions

This study calculates the spatiotemporal distribution mode of HDW in the YRB during summer from 1979 to 2022 further analyzes the detailed mechanisms by which the AAO affects the summer HDW in the YRB, and concludes as below:

- (1) A statistically significant correlation shows a positive phase between MJ AAO and JA PC3 of HDW in the YRB during summer. Preceding MJ AAO has a significant correlation to following JA HDW in the YRB, with a positive correlation in the western part of UYRB, and a negative correlation in the northeastern part of MYRB to LYRB.
- (2) The seasonal persistence of the AAO signal is handled by the underlying Southern Ocean, with key regions of SST anomalies in the South Atlantic and Southwestern Pacific reflecting as a SOSST pattern. MJ AAO imprinted itself into SOSST and was prolonged into late July–August by the oceanic memory. JA SOSST adjusted East

- Asian atmospheric circulation through the Rossby wave propagation and further affected simultaneous HDW in the YRB, as the lagging impact of MJ AAO.
- (3) JA SOSST induced an anticyclonic anomaly over the South Atlantic-South Indian Ocean, triggering wave dispersion splitting into two branches. One propagated eastward and equatorward through the Somalia-Tropical Indian Ocean tunnel, maintaining a negative phased EAP pattern, favoring northerlies anomaly along with the weakened high-latitude air invasion over the eastern YRB, resulting in the southerly domination. Another branch propagated directly equatorward through the Somali region, resulting in a positive geopotential height anomaly over the Urals-Western Asia, favoring the southeast invasion of high latitude air flow, weakening the moisture of the UYRB. Therefore, MJ AAO induced cross-equatorial planetary wave propagation through seasonal-persistent SOSST, leading to different moisture and temperature conditions, thereby HDW in the UYRB and MYRB-LYRB during late summer.
 - (4) The SST anomalies of the Southern Ocean, especially in the South Atlantic, have indications for the JA HDW in the YRB to some extent. Through the PLS method, the JA HDW in the YRB of 2022 was well reproduced by the SST anomalies of the Southern Ocean, with the anomaly consistency rate as 97.76%.

Supplementary Materials: The following supporting information can be downloaded at: <https://www.mdpi.com/article/10.3390/atmos15080998/s1>, Figure S1: Location of the study area (the observational stations); Figure S2: Monthly high-temperature days (left column) and no-precipitation days (right column) of June to September from 1961 to 2023 (Purple dotted line denotes climatology); Figure S3: Correlation coefficients between MJ AAO and JA HDW in the YRB from 1979 to 2022 (markers '+', 'x' and '*' are significant at 90%, 95% and 99% confident levels, respectively, red denotes positive while blue denotes negative); Figure S4. SVR predictive result of JA HDW in the YRB during 2022.

Author Contributions: Conceptualization, Z.Y. and Y.X.; methodology, Z.Y. and S.H.; software, Z.Y., L.D. and S.H.; validation, Z.Y., L.D. and Y.X.; formal analysis, Z.Y.; investigation, Z.Y.; resources, Z.Y. and L.D.; data curation, Z.Y. and L.D.; writing—original draft preparation, Z.Y.; writing—review and editing, Z.Y., L.D. and Y.X.; visualization, Z.Y. and L.D.; supervision, L.D. and Y.X.; project administration, J.Z. and L.D.; funding acquisition, J.Z. and L.D. All authors have read and agreed to the published version of the manuscript.

Funding: This research was primarily funded by the Hubei Provincial Natural Science Foundation Projects (2023AFD097). It also received support from the following sources: Study on the relationship between snow cover variation in the Qinghai–Tibet Plateau and multi-temporal and spatial precipitation in the Yangtze River Basin (2423020048), China Meteorological Administration Numerical Forecasting Unified Research and Development Project (TCYF2024QH006, TCYF2024GS034), China Meteorological Administration Innovation Development Special Project (CXFZ2023J051), Hubei Provincial Natural Science Foundation Projects (2022CFD014).

Institutional Review Board Statement: Not applicable.

Informed Consent Statement: Not applicable.

Data Availability Statement: Reanalysis Data and Model products are downloaded from '<https://psl.noaa.gov/data/gridded/data.ncep.reanalysis.html>', '<https://cds.climate.copernicus.eu/cdsapp#!/dataset/reanalysis-era5-pressure-levels-monthly-means>' and '<https://cds.climate.copernicus.eu/cdsapp#!/dataset/projections-cmip6?tab=form>' (accessed on 15 August 2024). Observational data of 700 stations in Yangtze River Basin are provided by Wuhan Regional Climate Center with the permission.

Conflicts of Interest: Author Jun Zhang was employed by the company China Yangtze Power Co., Ltd. The remaining authors declare that the research was conducted in the absence of any commercial or financial relationships that could be construed as a potential conflict of interest.

References

1. Xia, Z.; Liu, M.; Qin, P.; Fan, J.; Feng, Y.; Zhao, X. Development Process of High Temperature and Drought Events over Yangtze River Basin in 2022 and Assessment on Its Influences. *Yangtze River* **2023**, *54*, 21–28. (In Chinese) [[CrossRef](#)]
2. Gao, Y.; Xiao, Y.; Qin, P.; Xiong, K.; Liu, M. Climatic Characteristics and Analysis on the Causes of Summer Drought in the Upper Reaches of the Yangtze River Basin. *China Flood Drought Manag.* **2023**, *33*, 12–17. (In Chinese) [[CrossRef](#)]
3. Jiang, Y.; Hou, A.; Hao, Z.; Zhang, X.; Fu, Y.; Hao, F. Evolution of Hot Droughts in the Yangtze River Basin in 2022. *J. Hydroelectr. Eng.* **2023**, *42*, 1–9. (In Chinese)
4. Xia, J.; Chen, J.; She, D. Impacts and Countermeasures of Extreme Drought in the Yangtze River Basin in 2022. *J. Hydraul. Eng.* **2022**, *53*, 1143–1153. (In Chinese) [[CrossRef](#)]
5. Hao, L.; Ma, N.; He, L. Circulation Anomalies Characteristics of the Abnormal Drought and High Temperature Event in the Middle and Lower Reaches of the Yangtze River in Summer of 2022. *J. Arid Meteorol.* **2022**, *40*, 721–732. (In Chinese) [[CrossRef](#)]
6. Zhou, J.; Ren, H.; Wang, M.; Cui, T. Characteristics and Causes of Drought Event over Yangtze River Basin in Summer 2022. *Yangtze River* **2023**, *54*, 29–35. (In Chinese) [[CrossRef](#)]
7. Mei, M.; Gao, G.; Li, Y.; Wang, G.; Dai, T.; Chen, Y. Change Characteristics in Compound High Temperature and Drought Extreme Events over Yangtze River Basin from 1961 to 2022. *Yangtze River* **2023**, *54*, 12–20. (In Chinese) [[CrossRef](#)]
8. Fan, J.; Qin, P.; Shi, R.; Li, M.; Du, L. Characteristics of Compound Hot and Drought Disasters in Hubei under the Background of Climate Change. *J. Arid Meteorol.* **2022**, *40*, 780–790. (In Chinese) [[CrossRef](#)]
9. Azizi, H.; Nejatian, N. Evaluation of the Climate Change Impact on the Intensity and Return Period for Drought Indices of SPI and SPEI (Study Area: Varamin Plain). *Water Sci. Technol. Water Supply* **2022**, *22*, 4373–4386. [[CrossRef](#)]
10. Cai, W.; Liu, Y.; Zhai, J.; Wang, G.; Yan, J.; Chen, Y.; Wang, S. Climatic Anomalous Characteristics and Major Meteorological Disaster Events over China in Autumn 2021. *Meteorol. Sci. Technol.* **2023**, *51*, 56–65. [[CrossRef](#)]
11. Kazemzadeh, M.; Noori, Z.; Alipour, H.; Jamali, S.; Akbari, J.; Ghorbanian, A.; Duan, Z. Detecting Drought Events over Iran during 1983–2017 Using Satellite and Ground-Based Precipitation Observations. *Atmos. Res.* **2022**, *269*, 106052. [[CrossRef](#)]
12. Omar, A.A.; Chiang, J.-L.; Daud, B.H. Spatiotemporal Analysis of Meteorological Drought Using Standardized Precipitation Index (SPI) in Gabiley Region, Somaliland. *J. Geosci. Environ. Prot.* **2023**, *11*, 47–59. [[CrossRef](#)]
13. Zhou, Z. The Characteristics of the Circulation Causing Continuous High Temperature and Drought in the Yangtze and Huaihe River Valley in 1994. *Meteorol. Mon.* **1996**, *22*, 40–42. (In Chinese) [[CrossRef](#)]
14. Chen, L.; Zhou, L.; Dang, J.; Hu, Y.; Sheng, F. Research on Physical Mechanism of Summer Severe Climatic High Temperature and Drought Disasters in Sichuan and Chongqing Area in 2006. *Meteorol. Mon.* **2010**, *36*, 85–91. (In Chinese)
15. Deng, C.; She, D.; Zhang, L.; Zhang, Q.; Liu, X.; Wang, S. Characteristics of Drought Events Using Three-Dimensional Graph Connectedness Recognition Method in the Yangtze River Basin, China. *Trans. Chin. Soc. Agric. Eng.* **2021**, *37*, 131–139. (In Chinese) [[CrossRef](#)]
16. Zou, X.; Gao, R.; Chen, X.; Wang, L.; Li, W.; Gong, W.; Zhang, Q. Monitoring and Assessment of Summer Drought in the Yangtze River Basin in 2022. *China Flood Drought Manag.* **2022**, *32*, 12–16. (In Chinese) [[CrossRef](#)]
17. Sun, Z.; Zhang, Q.; Sun, R.; Deng, B. Characteristics of the Extreme High Temperature and Drought and Their Main Impacts in Southwestern China of 2022. *J. Arid Meteorol.* **2022**, *40*, 764–770. (In Chinese) [[CrossRef](#)]
18. Li, Y.; Zhang, J.; Yue, P.; Wang, S.; Zha, P.; Wang, L.; Sha, S.; Zhang, L.; Zeng, D.; Ren, Y.; et al. Study on Characteristics of Severe Drought Event over Yangtze River Basin in Summer of 2022 and Its Causes. *J. Arid Meteorol.* **2022**, *40*, 733–747. (In Chinese) [[CrossRef](#)]
19. Zhu, Z. An Analysis of Drought Event and Its Causation in Jianghuai Region During Summer 2013. *J. North China Inst. Aerosp. Eng.* **2016**, *26*, 37–40. (In Chinese)
20. Jiang, Y.; Hao, Z.; Feng, X.; Zhang, Y.; Zhang, X.; Fu, Y.; Hao, F. Spatiotemporal Evolution Characteristics in Compound Hot-Dry Events in Yangtze River and Yellow River Basins. *Water Resour. Prot.* **2023**, *39*, 70–77. (In Chinese) [[CrossRef](#)]
21. Wang, W.; Xu, J.; Cai, X.; Sun, C. Analysis of Atmospheric Circulation Characteristics and Mechanism of Heat Wave and Drought in Summer of 2013 over the Middle and Lower Reaches of Yangtze River Basin. *Plateau Meteorology* **2017**, *36*, 1595–1607. (In Chinese) [[CrossRef](#)]
22. Wei, N.; Gong, Y.; Miao, Q.; Deng, R. Analysis and Possible Cause of Heatwave over South China in 2013 Summer. *J. Chengdu Univ. Inf. Technol.* **2016**, *31*, 401–407. (In Chinese) [[CrossRef](#)]
23. Du, X. Atmosphere Anomaly of the Hot and Cool Summer over the Yangtze River Basin in China in Recent Years. Master's Thesis, Nanjing University of Information Science and Technology, Nanjing, China, 2018.
24. Feng, B.; Qiu, H.; Ji, G.L. Characteristics and Causes of Meteorological Drought over Changjiang River Basin in Summer of 2022. *Yangtze River* **2022**, *53*, 6–15. (In Chinese)
25. Sun, B.; Wang, H.; Huang, Y.; Yin, Z.; Zhou, B.; Duan, M. Characteristics and Causes of the Hot-Dry Climate Anomalies in China during Summer of 2022. *Trans. Atmos. Sci.* **2023**, *46*, 1–8. (In Chinese) [[CrossRef](#)]
26. Lin, S.; Li, H.; Huang, P.; Duan, X. Characteristics of High Temperature, Drought and Circulation Situation in Summer 2022 in China. *J. Arid Meteorol.* **2022**, *40*, 748–763. (In Chinese)
27. Fu, C.; Zeng, Z. The Connection between the North Atlantic Oscillation Index during Winter of the Last 530 Years and the East China Summer Drought-Flood Index. *Chin. Sci. Bull.* **2005**, *50*, 1512–1522. [[CrossRef](#)]

28. Yong, L.; Chen, H.; Li, H.; Wang, H. The Impact of Preceding Spring Antarctic Oscillation on the Variations of Lake Ice Phenology over the Tibetan Plateau. *J. Clim.* **2020**, *33*, 639–656. [[CrossRef](#)]
29. Nimac, I.; Herceg-Bulić, I.; Žuvela-Aloise, M.; Žgela, M. Impact of North Atlantic Oscillation and Drought Conditions on Summer Urban Heat Load—A Case Study for Zagreb. *Int. J. Climatol.* **2021**, *42*, 4850–4867. [[CrossRef](#)]
30. Wang, S.; Wu, Q.; Liu, S.; Liang, H.; Hu, Y.; Kang, C.; Bao, X.; Gao, Y. Impacts of Antarctic Sea Ice Oscillation on Boreal Summer Atmospheric Circulation in the Northern Hemisphere. *Chin. J. Atmos. Sci.* **2022**, *46*, 1349–1365. (In Chinese) [[CrossRef](#)]
31. Li, J.; Ren, H.; Lu, B.; Liu, J.; Kang, Y. Collaborative Effects of Phase Configurations of North Atlantic Oscillation and Southern Annular Mode on Summer Precipitation Anomalies over Southern China. *Chin. J. Geophys.* **2017**, *60*, 3730–3744. (In Chinese) [[CrossRef](#)]
32. Xue, F.; Guo, P.; Yu, Z. Influence of Interannual Variability of Antarctic Sea-Ice on Summer Rainfall in Eastern China. *Adv. Atmos. Sci.* **2003**, *20*, 97–102. [[CrossRef](#)]
33. Gao, H.; Liu, Y.Y.; Wang, Y.G.; Li, W.J. Precursory Influence of the Antarctic Oscillation on the Onset of Asian Summer Monsoon. *Chin. Sci. Bull.* **2013**, *58*, 678–683. [[CrossRef](#)]
34. Zheng, F.; Li, J.; Clark, R.T.; Ding, R.; Li, F.; Wang, L. Influence of the Boreal Spring Southern Annular Mode on Summer Surface Air Temperature over Northeast China. *Atmos. Sci. Lett.* **2015**, *16*, 155–161. [[CrossRef](#)]
35. Wang, H.; Fan, K. Zonal Winds at the Upper Troposphere of the Southern Hemisphere and the Atmospheric Circulation of the East Asian Summer Monsoon. *Chin. Sci. Bull.* **2006**, *51*, 1595–1600. (In Chinese) [[CrossRef](#)]
36. Wang, H.; Fan, K. The Relationship between the Formation Frequency of Typhoon in the Northwest Pacific and the Antarctic Oscillation. *Chin. Sci. Bull.* **2006**, *51*, 2910–2914. (In Chinese) [[CrossRef](#)]
37. Huang, S.; Qin, J.; Li, S.; Yuan, Z.; Mbululo, Y. Spatiotemporal Variability of the Southern Second Mode and Its Influence on June Precipitation in Southern China. *J. Geophys. Res. Atmos.* **2022**, *127*, e2022JD036762. [[CrossRef](#)]
38. Kalnay, E.; Kanamitsu, M.; Kistler, R.; Collins, W.; Deaven, D.; Gandin, L.; Iredell, M.; Saha, S.; White, G.; Woollen, J.; et al. The NCEP/NCAR 40-Year Reanalysis Project. *Bull. Am. Meteorol. Soc.* **1996**, *77*, 437–471. [[CrossRef](#)]
39. Haenlein, M.; Kaplan, A.M. A Beginner's Guide to Partial Least Squares Analysis. *Underst. Stat.* **2004**, *3*, 283–297. [[CrossRef](#)]
40. Zhang, Z.; Gong, D.; Mao, R.; Qiao, L.; Kim, S.J.; Liu, S. Possible Influence of the Antarctic Oscillation on Haze Pollution in North China. *J. Geophys. Res. Atmos.* **2019**, *124*, 1307–1321. [[CrossRef](#)]
41. Luo, F.; Li, S.; Gao, Y.; Keenlyside, N.; Svendsen, L.; Furevik, T. The Connection between the Atlantic Multidecadal Oscillation and the Indian Summer Monsoon in CMIP5 Models. *Clim. Dyn.* **2018**, *51*, 3023–3039. [[CrossRef](#)]
42. Takaya, K.; Nakamura, H. A Formulation of a Phase-Independent Wave-Activity Flux for Stationary and Migratory Quasi-geostrophic Eddies on a Zonally Varying Basic Flow. *J. Atmos. Sci.* **2001**, *58*, 608–627. [[CrossRef](#)]
43. Zhao, S.; Li, J.; Li, Y. Dynamics of an Interhemispheric Teleconnection across the Critical Latitude through a Southerly Duct during Boreal Winter. *J. Clim.* **2015**, *28*, 7437–7456. [[CrossRef](#)]
44. Yang, S.; Deng, K.; Ting, M.; Hu, C. Advances in Research on Atmospheric Energy Propagation and the Interactions between Different Latitudes. *J. Meteorol. Res.* **2015**, *29*, 859–883. [[CrossRef](#)]
45. Li, Y.; Li, J. Propagation of Planetary Waves in the Horizontal Non-Uniform Basic Flow. *Chin. J. Geophys.* **2012**, *55*, 361–371. (In Chinese) [[CrossRef](#)]
46. Zhang, H.; Qin, J.; Li, Y. Climatic Background of Cold and Wet Winter in Southern China: Part I Observational Analysis. *Clim. Dyn.* **2011**, *37*, 2335–2354. [[CrossRef](#)]
47. Yuan, Z.; Qin, J.; Li, S.; Huang, S.; Mbululo, Y.; Rehman, A. Impact of Boreal Autumn Antarctic Oscillation on Winter Wet–Cold Weather in the Middle–Lower Reaches of Yangtze River Basin. *Clim. Dyn.* **2022**, *58*, 329–349. [[CrossRef](#)]
48. Yuan, Z.; Qin, J.; Du, L.; Huang, S.; Wang, Y.; Mbululo, Y. The Role of Antarctic Sea Ice in Modulating the Relationship between September–October Antarctic Oscillation and Following January–February Wet and Cold Weather in Southern China. *Int. J. Climatol.* **2023**, *43*, 3605–3628. [[CrossRef](#)]
49. Sun, X.; Li, S.; Yu, Y.; Guo, D.; Shi, C. Climate Characteristics of Winter Long-Lasting Freezing Rain and Snow Events in South China from 1951 to 2017 and Their Relationship with Circulation Anomalies. *Trans. Atmos. Sci.* **2022**, *45*, 768–777. (In Chinese) [[CrossRef](#)]
50. Yuan, Z.; Qin, J.; Li, S.; Huang, S.; Mbululo, Y. Impact of Spring AAO on Summertime Precipitation in the North China Part: Observational Analysis. *Asia-Pac. J. Atmos. Sci.* **2020**, *57*, 1–16. [[CrossRef](#)]
51. Sun, J. Possible Impact of the Boreal Spring Antarctic Oscillation on the North American Summer Monsoon. *Atmos. Ocean. Sci. Lett.* **2010**, *3*, 232–236. [[CrossRef](#)]
52. Liu, T.; Li, J.; Feng, J.; Wang, X.; Li, Y. Cross-Seasonal Relationship between the Boreal Autumn SAM and Winter Precipitation in the Northern Hemisphere in CMIP5. *J. Clim.* **2016**, *29*, 6617–6636. [[CrossRef](#)]
53. Chang, L.; Wu, Z.; Xu, J. Potential Impacts of the Southern Hemisphere Polar Vortices on Central-Eastern China Haze Pollution during Boreal Early Winter. *Clim. Dyn.* **2020**, *55*, 771–787. [[CrossRef](#)]
54. Shi, W.; Xiao, Z.; Xue, J. Teleconnected Influence of the Boreal Winter Antarctic Oscillation on the Somali Jet: Bridging Role of Sea Surface Temperature in Southern High and Middle Latitudes. *Adv. Atmos. Sci.* **2016**, *33*, 47–57. [[CrossRef](#)]
55. Zhang, D.; Jin, F.; Li, J.; Ding, R. Enhancement of North Atlantic Oscillation by Transient Eddies. *Chin. J. Atmos. Sci.* **2011**, *35*, 927–937.

-
56. Liu, T.; Li, J.; Zheng, F. Influence of the Boreal Autumn Southern Annular Mode on Winter Precipitation over Land in the Northern Hemisphere. *J. Clim.* **2015**, *28*, 8825–8839. [[CrossRef](#)]
 57. Wu, Z.; Dou, J.; Lin, H. Potential Influence of the November–December Southern Hemisphere Annular Mode on the East Asian Winter Precipitation: A New Mechanism. *Clim. Dyn.* **2015**, *44*, 1215–1226. [[CrossRef](#)]

Disclaimer/Publisher’s Note: The statements, opinions and data contained in all publications are solely those of the individual author(s) and contributor(s) and not of MDPI and/or the editor(s). MDPI and/or the editor(s) disclaim responsibility for any injury to people or property resulting from any ideas, methods, instructions or products referred to in the content.